Ce-doped strontium cobalt ferrite perovskites as cathode catalysts for solid oxide fuel cells: Effect of dopant concentration

Hyunkyu Choi, Anshuman Fuller, Jonathan Davis, Christopher Wielgus, Umit S. Ozkan*

William G Lowrie Department of Chemical and Biomolecular Engineering, The Ohio State University, Columbus, OH 43210, USA

ABSTRACT

The bulk structure, oxygen mobility, and button cell performance of perovskite-type oxides with the formula $Sr_{1-x}Ce_xCo_{0.2}Fe_{0.8}O_{3-\delta}$ for $x = 0.10$, 0.15, and 0.20 have been investigated using in situ X-ray diffraction (XRD), oxygen temperature-programmed desorption (O_2-TPD), CO_2-temperature-programmed oxidation (TPO) and button cell/impedance measurements. XRD results indicate that cerium-doped perovskites have a cubic structure and do not undergo structural changes with increasing temperature. An additional CeO_2 phase was observed when the concentration of Ce exceeded 15%. Addition of cerium lowers the thermal expansion coefficient (TEC), bringing the TEC closer to that of gadolinia-doped ceria (GDC) electrolyte. The oxygen vacancy generation was inversely proportional to the doping concentration of Ce. However, the best unit cell performance and the lowest impedance were achieved with intermediate levels of Ce doping, suggesting that the ceria phase which segregates at higher doping levels has a detrimental effect on the cell performance. CO_2-TPO experiments which were used to examine the rate of intra-facial transport of oxygen were found to be a good probe for button cell performance.

© 2012 Elsevier B.V. All rights reserved.

1. Introduction

Perovskite-type materials are mixed metal oxides with the general formula ABO_3 where the A ions can be rare earth metals which occupy dodecahedral sites, while the B ions can be transition metals which occupy octahedral sites. The broad diversity of the metallic elements that can form stable perovskite-type oxides can be applied in the design of new high performance catalysts for several applications. These materials are widely studied for their application as oxygen sensors and oxygen separation membranes, due to their ionic conductive properties [1,2]. They have also been studied as automotive exhaust catalysts where both total and partial oxidation catalytic activity can be utilized [3,4]. Their mixed ionic and electronic conductive properties have made perovskite oxides one of the most promising cathode materials for solid oxide fuel cells (SOFCs) [5,6].

The principal role of the SOFC cathode is to form oxide ions by the reduction of oxygen. The generated oxide ions travel through the electrolyte to the anode, where they undergo oxidation to produce electricity and water. Therefore, the performance of the cathode is limited by the surface oxygen exchange kinetics of the oxygen reduction reaction (ORR) as well as the bulk oxide ion

mobility [7]. These properties are expected to depend upon the surface and bulk structure, where oxygen vacancies provide the active sites for the ORR and the pathway of oxide ions to travel by random 'hopping' through the vacancies, respectively. An oxygen vacancy is formed by a charge imbalance in the material. Substituting the normally trivalent A-site with a divalent or tetravalent cation creates those charge imbalances in the perovskite. B-site transition metals also impact the oxygen vacancy formation. Co-, Fe- and Mn-based perovskites were studied and the oxygen vacancy formation was found to increase in the order of Co, Fe and Mn, respectively [8–10].

Our previous studies have focused on the effect of A- and B-site dopant concentration in $LaFeO_3$ [11–15]. Nonlinear dependence of oxygen vacancy generation and oxygen exchange kinetics on Co loading was found due to an electronic structure transition at high Co concentrations. Additional doping of the B-site with aliovalent cations (e.g. Zn, Ni, and Cu) increased the oxygen vacancy creation in the order of Zn > Ni > Cu. Increased Sr loading enhanced oxygen vacancy generation, however the mismatch between the yttria-stabilized zirconia (YSZ) electrolyte and the catalysts also increased due to the thermal expansion coefficient (TEC) incompatibility between the components.

The present work examines the effect of Ce doping in $SrCo_{0.2}Fe_{0.8}O_{3-\delta}$ (SCF) materials. Mixed conductive composites close to the brownmillerite stoichiometry (e.g. $Sr(CoFe)O_{2.5}$) exhibit high oxygen permeability at high temperatures ($T > 800\,°C$), but due to their structural changes at intermediate

* Corresponding author. Tel.: +1 614 292 6623.
  E-mail address: ozkan.1@osu.edu (U.S. Ozkan).

temperatures (650–750 °C), the oxide ion conductivity decreases. However, incorporating a small amount of CeO_2 into the framework could promote increased stability of the structure while maintaining high oxide ion mobility [16]. This work investigates the oxygen vacancy generation, oxygen mobility and thermal compatibility with the electrolyte as well as actual SOFC button cell performance with different Ce loadings in the A-site.

2. Experimental

2.1. Catalyst synthesis

The $Sr_{1-x}Ce_xCo_{0.2}Fe_{0.8}O_{3-\delta}$ samples were synthesized by the EDTA-citrate complexing method using metal nitrate precursors. Stoichiometric amounts of $Sr(NO_3)_2$ (Alfa Aesar), $Co(NO_3)_2 \cdot 6H_2O$ (Acros), $Fe(NO_3)_3 \cdot 6H_2O$ (Aldrich), $Ce(NO3)_3 \cdot 6H_2O$ (Fisher Scientific) or $La(NO_3)_3 \cdot 6H_2O$ (Aldrich) were dissolved in distilled water. EDTA was added to the mixed metal nitrate solution under stirring, and an NH_4OH solution was added to adjust the pH value at 6. Citric acid was added to the mixture when the temperature reached 60 °C. The mole ratio of metal ions to EDTA and metal ions to citric acid was 1:1 and 1:1.5, respectively. The mixed solution was then heated to 90 °C under magnetic stirring, until a brown gel was formed. The gel was kept overnight in an oven at 150 °C to dry the precursor. The dried precursors were subsequently ground with a mortar and a pestle and calcined in air at 1100 °C for 5 h for the perovskite formation to take place.

2.2. X-ray diffraction (XRD)

In situ X-ray powder diffraction patterns were recorded with a Bruker D8 Advance diffractometer using a Cu K_α radiation source ($\lambda = 1.5046$ Å, 40 kV and 50 mA). The instrument is equipped with an (Anton Paar) HTK 1200 sample chamber, capable of controlling the environment at a specified temperature. The diffractometer is equipped with an incident beam Ge (1 1 1) monochromator, incident beam Soller slits, and a Braun position-sensitive detector (PSD). The measurements were made with the HTK 1200 oven equipped with graphite windows. Samples were loaded on a 0.5 mm deep alumina holder. Data were acquired for 2θ values from 20° to 90° at a step size of 0.0144 with a dwell time of 1 s. A ramp rate of 10 °C/min and a 20 min hold time was employed prior to data acquisition at each temperature. Unit cell parameters were determined using a least-square fit.

2.3. Thermogravimetric analysis (TGA)

Thermogravimetric analysis of the samples was conducted using a Setaram TG-DSC 111. The instrument is capable of simultaneous microgravimetry and scanning calorimetry measurements. Flow balancing of the instrument in He at room temperature was performed prior to each set of experiments. The samples (~45 mg) were loaded in a Pt crucible and heated to 750 °C at 5 °C/min in 30 cm^3 of He and held for 30 min before being cooled to room temperature. Prior to the TPD, the samples were oxidized in 10%O_2/He at 750 °C for 30 min. The mass change was used to calculate the oxygen vacancy generation of the material, as discussed in our previous work [13].

2.4. Temperature programmed desorption (TPD) of oxygen

The experiment was performed on an Autochem II 2920 instrument connected to a Cirrus RGA-MS (MKS Instruments) operated in selected ion mode with a Faraday cup detector. 100 mg of catalyst sample was loaded on top of quartz wool in a fused quartz reactor. The samples were first pre-treated in an oxygen environment (30 cm^3 of 10%O_2/He) at 750 °C with an isothermal hold for 30 min and then cooled to room temperature under the same flow. After the sample was cooled to near room temperature, the flow was switched to 30 cm^3 He and the reactor was purged for an additional 1 h and 30 min to allow for the Mass Spectrometer (MS) signals to stabilize. The temperature was then increased from 50 to 900 °C using a linear temperature program at 5 °C/min and held for 30 min. The desorption products were monitored using the mass spectrometer. Peak integration/deconvolution was performed using Grams AI software.

2.5. Temperature programmed oxidation (TPO) with CO_2

CO_2-TPO experiments were conducted using an Autochem II 2920 instrument connected to a mass spectrometer (Cirrus RGA-MS, MKS Instruments). The samples were loaded into a quartz reactor and reduced with 30 cm^3 of 5%H_2/He at 850 °C for 30 min and subsequently cooled to room temperature. Once room temperature was reached, the gas flow was switched to 30 cm^3 He and purged for an hour. After an additional 30 min to stabilize the MS signals, the TPO experiment was run with 30 cm^3 of 10%CO_2/He using a linear temperature program with a ramp rate of 10 °C/min up to 850°, followed by an isothermal hold for 30 min. Peak integration was performed using Grams AI software.

2.6. Button cell preparation

A commercial scandia-stabilized zirconia (ScZ) tape (ESL ElectroScience) was used to make an electrolyte-supported SOFC cell. A circular disk (1.4 cm dia.) was punched from the ScZ tape and sintered at 1400 °C for 2 h for densification. NiO–YSZ supplied by Nextech Materials in powder form was used as the anode. The sample as received was 60% NiO and 40% 8YSZ on a mass basis. The YSZ portion of the sample was 92% zirconia and 8% yttria (8YSZ) on a molar basis. The anode powder was mixed with α-terpineol (SAIC), ethyl cellulose (Aldrich), which was used as a binder and a solvent mixture of toluene and ethanol in order to prepare a slurry, which was stirred for 10 h using a magnetic stirrer to achieve a homogeneous composition. It was then brush-painted onto the densified ScZ electrolyte with a controlled area of ~0.15 cm^2 and fired at 1200 °C for 5 h. The cathode slurries of $Sr_{1-x}Ce_xCo_{0.2}Fe_{0.8}O_{3-\delta}$ and $La_{0.6}Sr_{0.4}Co_{0.2}Fe_{0.8}O_{3-\delta}$ (LSCF-6428) were made using the same additives mentioned above and pasted after the anode side was sintered. The area of the cathode and the sintering conditions were the same as those employed for the anode. Ag current collectors were pasted on both electrodes using Ag paste.

2.7. Current–voltage and AC impedance measurements in SOFC button cell

The polarization curve was obtained at 800 °C using the SP-150 Potentiostat/Galvanostat (BioLogic Science Instruments) with Electrochemical Impedance Spectroscopy (EIS) capability. Pure H_2 at a flow rate of 80 cm^3 was introduced at the anode while house air was used on the cathode side. Prior to the measurement, stabilization of the polarization curve was achieved by a fast scan of the voltage from the open circuit voltage (OCV) to 0.1 V with a scan rate of 40 mV/s. Then the measurement was acquired from OCV to 0.1 V at a scan rate of 10 mV/s. The AC impedance spectra were obtained using the same instrument over a frequency range of 0.1 Hz–600 KHz at the OCV. The AC impedance measurements were conducted under the same operating condition as that used for the polarization curves.
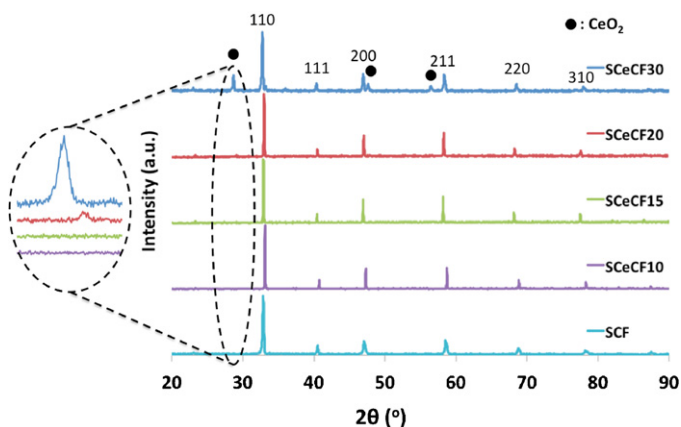
Fig. 1. XRD patterns of cerium-doped perovskites.

3. Results and discussion

3.1. Bulk structure properties

The bulk structure of $Sr_{1-x}Ce_xCo_{0.2}Fe_{0.8}O_{3-\delta}$ ($x = 0$, 0.1, 0.15, 0.2 and 0.3) catalysts under ambient conditions was determined using X-ray diffraction. The diffraction pattern of the baseline $SrCo_{0.2}Fe_{0.8}O_{3-\delta}$ (SCF) catalyst is also shown as a reference. As shown in Fig. 1, XRD patterns confirm the presence of a single-phase perovskite structure in samples containing a cerium doping level of 15%, and below, in the A-site. The diffraction patterns show a single, sharp peak, which is the characteristic diffraction line associated with a cubic perovskite structure. The tolerance factor, "t", is used to predict the perovskite structure formation with the range of 0.8–1, where r_A, r_B, and r_O are the ionic radii of A, B, and the oxide ion, respectively.

$$t = \frac{(r_A + r_O)}{\sqrt{2}(r_B + r_O)}$$

As the value of "t" approaches 1, the crystal structure is expected to be closer to the ideal cubic symmetry [17]. The calculated tolerance factors for all the cerium-doped perovskites were close to unity, indicating the presence of the cubic structure, which is also verified from the XRD data.

As the cerium doping level exceeds 15%, a small peak due to unreacted CeO_2 appears and its intensity increases with the addition of cerium. There have been earlier reports where perovskites with $LaMO_3$ (M: Co or Fe) formulas were modified with cerium doping where the maximum amount of cerium that could be doped into the A-site was reported to be between 5 and 10% [18–20]. In this case, having strontium as the primary cation, which brings a different charge balance and more similar ionic sizes, appears to allow a higher dopant level incorporation in the A-site. Overall, the synthesis procedure was successful in introducing cerium into the catalyst bulk without affecting the perovskite structure.

The high temperature bulk structure of the perovskite was also investigated via in situ XRD. The crystal structure is an important factor determining the oxygen activation and mobility in these materials. Our previous studies with cobalt-doped lanthanum ferrite samples, including those with a second transition metal such as Zn in the B-site, showed rhombohedral structure at room temperature and a phase transition from rhombohedral to cubic with an increase in temperature [13,14]. Among these different phases, the cubic phase is known to have more symmetry than the rhombohedral phase, leading to an increased random distribution of the vacancies resulting in higher oxide ion mobility. The diffraction patterns for the main cubic Miller indices (1 1 1) are shown in Fig. 2.
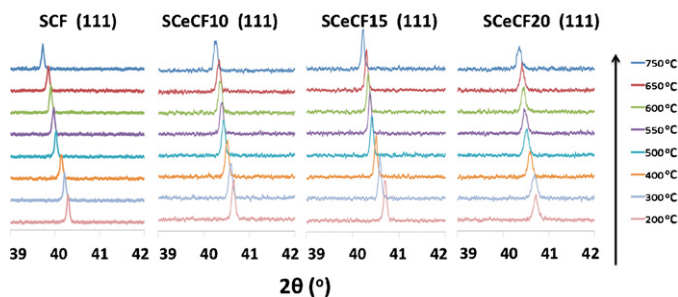

Fig. 2. Diffraction patterns of cerium-doped perovskite as a function of temperature in air.
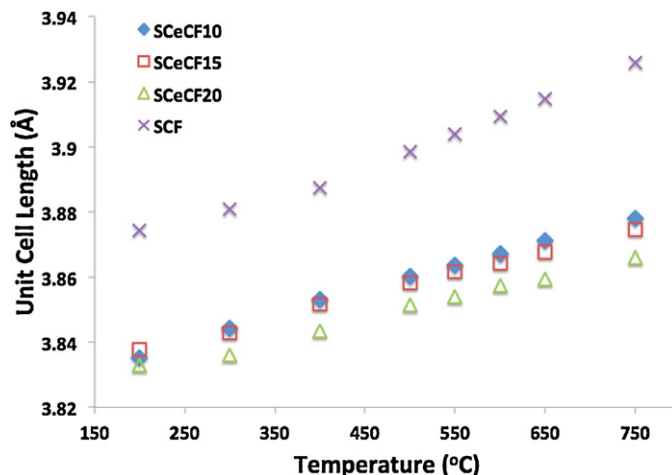

Fig. 3. Unit cell parameters for cerium-doped perovskites as a function of temperature in air.

For all cerium-doped perovskites studied as well as SCF, no phase transition was observed and the cubic structure remained intact with a rise in temperature. This was confirmed based on the presence of a single sharp peak. With increasing temperature, the peak in all the samples became sharper and shifted to lower 2-θ values indicating thermal expansion. The unit cell length is expected to increase linearly with temperature based on the concept of linear thermal expansion. Unit cell lengths were calculated using the Bragg's formula for the Miller indices (1 1 0) from the XRD patterns shown in Fig. 3. Calculations were repeated using (2 0 0), (2 2 0) and (2 1 1) diffraction lines and the average percent error was found to be around 0.4%. As seen from the slopes in the figure, thermal expansions of these materials appear to be constant over a wide temperature range.

Table 1 presents the TEC of each sample and compares them to the TECs of potential SOFC electrolytes, which were calculated using the same technique. In view of the long-term operation of SOFCs, thermal compatibility between the electrodes and the electrolyte is vital because a large difference will generate stresses within the cell, eventually leading to cracking or degradation of the electrode

Table 1
Thermal expansion coefficient values calculated from in situ XRD patterns.

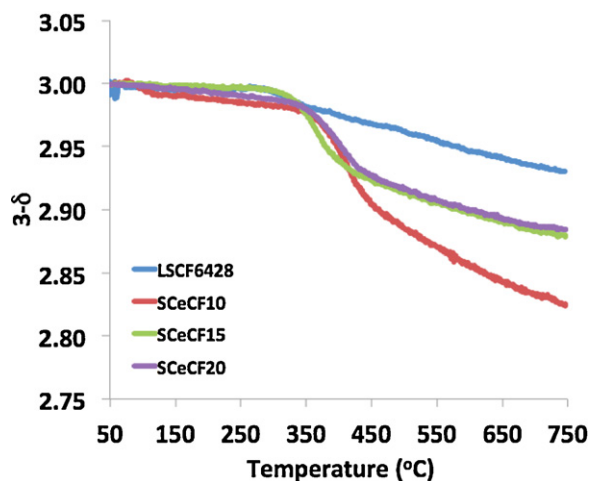|	TEC (ppm/°C)
SCF	25
SCeCF10	20
SCeCF15	18
SCeCF20	16
Ceria (GDC)	13
Zirconia (YSZ)	9

Fig. 4. Temperature-programmed oxygen evolution in inert(He) environment measured using TGA.

[21]. As seen from the table, the TEC of cerium-free SCF sample is the highest and the TECs decrease with increasing cerium doping level and get closer to the TEC of the GDC electrolyte. This trend may be attributed to the chemical expansion in addition to the thermal expansion of the samples. With an increase in temperature, transition metals in the B-site of perovskite oxides may be chemically reduced, ultimately generating oxygen vacancies [22]. The change in oxidation states of the transition metal (e.g. +4 to +3) induces a change in the lattice volume while maintaining its phase. In the case of the cerium-doped samples, some of the B-site metals will be in +3 state, hence reducing the number of transition metal atoms with the +4 oxidation state. This, in turn, will decrease the chemical expansion that could take place due to the reduction of transition metals with +4 oxidation state at higher temperature.

The large thermal incompatibility observed between the electrolyte and SCF led us to conclude that cerium-free SCF samples do not offer any potential to be used as cathode materials and hence, the remaining part of the results focuses only on Ce-doped catalysts.

3.2. Temperature-programmed desorption of oxygen (O_2-TPD)

The generation of oxygen vacancies is an important parameter for determining the oxygen reduction reaction (ORR) activity of a catalyst. Thermogravimetric analysis, which was performed in an inert atmosphere, was used to investigate the evolution of oxygen from the prepared catalysts as a function of temperature (Fig. 4). All of the Ce-doped catalysts exhibit a higher oxygen vacancy content compared to that of the LSCF-6428. The oxygen vacancy generation was found to be the highest for the sample with the lowest Ce loading level (SCeCF10). This can be explained by the fact that the amount of tetravalent transition metals in the B site is highest for the SCeCF10 and decreases with increasing Ce loading levels. Since Co and Fe are less stable in the +4 oxidation state, at higher temperatures, they partially convert to a +3 oxidation state and the resulting charge imbalance is compensated by increased oxygen vacancies. Out of the three cerium-doped samples, the amount of oxygen that evolved for 15%- and 20%-cerium-doped catalysts was observed to be very similar to each other. From the ex situ XRD data, the maximum amount of cerium that could be doped in the catalysts was found to be between 15% and 20%. Cerium doping at higher levels cannot be incorporated into the A-site and leads to the formation of a separate CeO_2 phase. If the same amount of cerium was doped in the A-site for both SCeCF15 and SCeCF20 perovskites, this would result in a similar level of oxygen vacancy generation for these two catalysts.
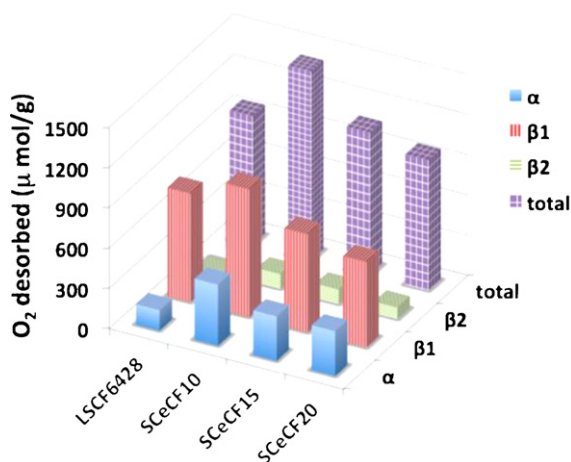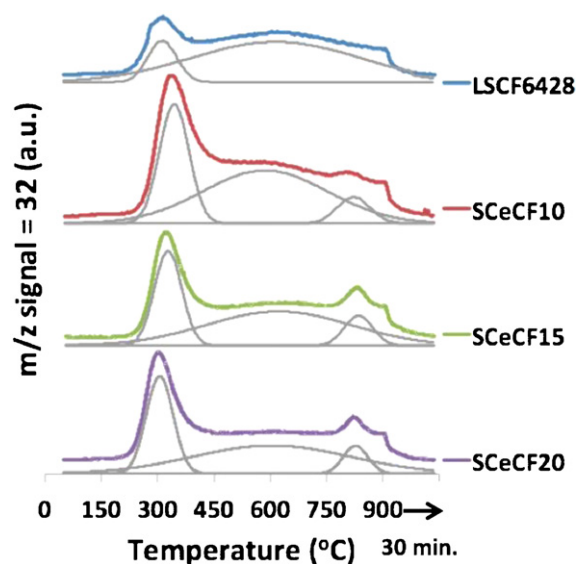

Fig. 5. (a) Temperature-programmed oxygen evolution in inert(He) environment monitored using mass spectrometry, (b) O_2 desorbed calculated from the TPD profiles.

The temperature-programmed desorption of O_2 was further examined using mass spectrometry. The O_2-TPD profiles of the cerium-doped catalysts showed two distinct and temperature-dependent oxygen evolution peaks, a low temperature one at ~450 °C and a high temperature one above 450 °C, indicating that the oxygen species may exist in different matrices in the sample. Fig. 5a shows the O_2-TPD profiles of the cerium-doped catalysts under an inert atmosphere. The experiments were performed with a mass spectrometer in selected ion mode to trace the relevant ions. After the appropriate pretreatment of the samples, the amount of oxygen evolved was quantified using the $m/z = 32$ signal and is shown in Fig. 5b. Generally, two types of oxygen evolving from perovskites have been reported in the literature. As outlined by Seiyama earlier [23], the perovskite structures with A or B site substitution form many lattice defects and these defects are thought to play a role in increasing the oxygen "absorption" characteristics of these materials. "Absorbed" oxygen in these materials, which is weakly bound to the cations behaves differently from oxygen which is part of the crystal lattice, and is more readily accessible. In the TPD profiles, the low temperature peak observed below 450 °C (α-oxygen), is thought to be due to the evolution of absorbed oxygen present in the materials as well as surface-adsorbed oxygen. The SCeCF10 catalyst showed the highest amount of desorbed α-oxygen followed by SCeCF15 and SCeCF20, which show equal

amounts of α-oxygen desorption. If the A-site doping determines the amount of α-oxygen desorbed, this result is consistent with our earlier findings which showed that the maximum amount of Ce that could be incorporated in the A site may be around 15%. If this is the case, SCeCF15 and SCeCF20 would both have the same level of A-site substitution. The amount of α-oxygen evolved far exceeded the amount that could be present in a surface mono-layer (4.0 μmol O$_2$ m^{-2} for a monolayer), indicating that most of the evolved α-oxygen that desorbed was associated with the bulk.

As seen in Fig. 5, the Ce-doped catalysts exhibited a broad temperature range for the high-temperature oxygen evolution. This feature denoted as β-oxygen in the literature is thought to be associated with the partial reduction of the transition metal in the B-site and is linked to the anionic mobility in these materials [24–26].

Earlier reports from the literature as well as some of our own work have shown the La$_{0.6}$Sr$_{0.4}$Co$_x$Fe$_{1-x}$O$_{3-\delta}$ ($x = 0.2, 0.4, 0.6$) catalysts to display a single β-oxygen desorption peak above 450 °C [12,13,24,26,27] during oxygen TPD in an inert environment. The cerium-doped samples examined in this study, however, showed the evolution of an additional β-oxygen desorption feature above 800 °C. This feature could possibly be due to the presence of cerium in the A-site partially stabilizing the transition metals in the B-site. It is also conceivable that the β1 and β2 features stem from the two different cations (i.e., Co and Fe) occupying the B-site and showing different levels of propensity toward reduction. It is also possible that they correspond to the reduction of tetravalent and trivalent cations, respectively. The fact that the amount of oxygen desorbing with the β1 feature decreases with increasing cerium doping is consistent with this possibility since cerium doping is expected to decrease the abundance of tetravalent cations to preserve the charge neutrality. The results in this study, however, do not allow a definitive assignment to the source of the β1 and β2 oxygen features. The LSCF-6428 sample that was included for comparison showed the lowest oxygen desorption among all the samples, both in total and in the individual α and β features.

3.3. CO$_2$-temperature programmed oxidation (CO$_2$-TPO)

The ORR at an SOFC cathode involves multiple steps: (1) adsorption of diatomic oxygen species on to the surface active sites, (2) dissociation to produce monoatomic species and (3) interfacial transport of the surface oxygen to the catalyst bulk. CO$_2$ temperature-programmed oxidation can be an indicator of the ORR activity of SOFC cathode catalysts since the steps involved are similar to those of the ORR, namely dissociative adsorption of CO$_2$ followed by filling the surface oxygen vacancies and/or transportation of monoatomic oxygen into the bulk lattice. Therefore, the activity of the catalysts for CO$_2$ adsorption and dissociation can provide information, at least qualitatively, of the ease with which the surface oxygen can move into the perovskite lattice [28,29]. Fig. 6 illustrates the CO ($m/z = 28$) signal from the CO$_2$-TPO experiments for cerium-doped catalysts. Also included in the figure is the CO signal for LSCF-6428 catalyst for comparison. From Fig. 6, it is apparent that there are two distinct features in the CO$_2$-TPO profile, a sharp peak at around 650 °C, and a broad shoulder at higher temperatures over 850 °C. These features seen in the CO evolution profile are possibly associated with different sites and vacancies on the catalyst surface as well as in the bulk. At high temperatures ($T > 850$ °C), especially, the SCeCF10 catalyst showed a relatively smaller CO evolution when compared to other catalysts, indicating the presence of vacant sites that are harder to re-oxidize. A large amount of CO evolution is indicative of an increased activity of CO$_2$ dissociation along with an increase in the amount of surface oxygen transported to the bulk. Although SCeCF10 shows slower oxygen transportation at high temperature, the overall peak area in terms of the total amount of CO evolution shows the
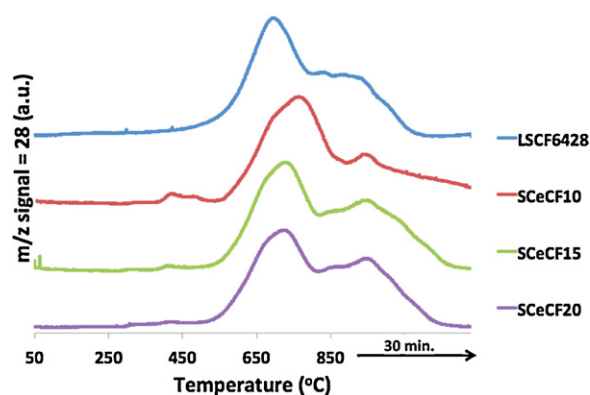

Fig. 6. CO$_2$-TPO profile for LSCF6428; SCeCF10; SCeCF15; SCeCF20.

Table 2
Total amount of CO formation during CO$_2$-TPO.

μmol/g	LSCF 6428	SCeCF 10	SCeCF 15	SCeCF 20
Total	1893	1917	2128	1902

trend SCeCF15 > SCeCF10 > SCeCF20 > LSCF-6428 and is presented in Table 2. These results indicate that the oxygen transport rate increases with increasing cerium concentration in the A-site of the catalysts. The reason that SCeCF20 had a slower oxygen transportation rate compared to the other cerium-doped catalysts could possibly be caused by the presence of a secondary phase (CeO$_2$).

3.4. Button cell performance

Electrolyte-supported button cells were fabricated using three different levels of cerium doping on the cathode, SCeCF10, SCeCF15, SCeCF20. The current (I) versus voltage (V) and power density profiles for these button cells operating with H$_2$ at 800 °C are shown in Fig. 7. The data obtained from LSCF-6428 are also included for comparison. The V–I curves for the button cells show that the best performance was achieved by SCeCF10 and SCeCF15. These are the samples that showed the highest oxygen vacancy formation and the highest CO$_2$ reduction activities, as discussed in the O$_2$-TPD and CO$_2$-TPO results section above. A high propensity for oxygen vacancy creation signals a higher ability for oxide ion conduction. CO$_2$-TPO provides an insight into the rates of oxygen dissociation and transportation of surface oxygen to the bulk. Although the samples with intermediate cerium loading levels perform the best (and significantly better than LSCF), the sample with a higher loading level (SCeCF20) exhibits the poorest performance. One possible
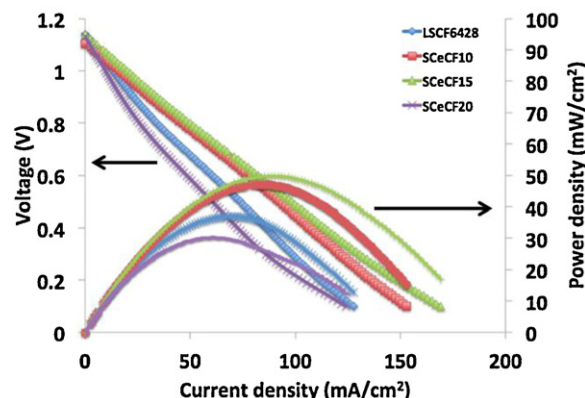

Fig. 7. Voltage and power density vs. current density at 800 °C.
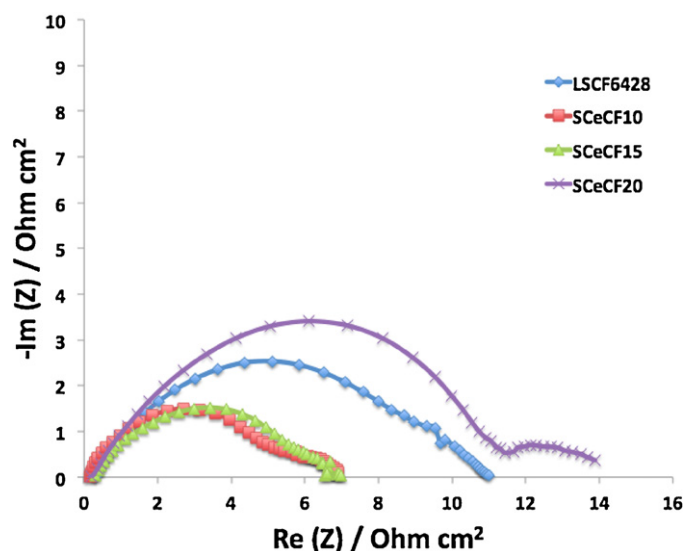
Fig. 8. OCV electrochemical impedance spectra at 800 °C.

explanation is the existence of a CeO_2 phase, segregating out of the perovskite structure. This phase is not likely to contribute to the ORR activity. On the contrary, it is possible that the CeO_2 phase hinders ionic conduction in the material. The very low CO formation data from CO_2-TPO experiment signals a slow bulk transport of oxygen in this sample.

The AC impedance spectra for each cell at the OCV are shown in Fig. 8. The spectra show that the decrease in performance was followed by an increase in the area specific resistance (ASR) of the cell, which corresponds to the overall width of the arcs. As identified by X-ray diffraction, the presence of a secondary phase (CeO_2) with low electrical and/or ionic conductivity, in SCeCF20 is seen to increase the overall impedance of the button cell and is consistent with the SCeCF20 exhibiting the poorest performance among all the catalysts tested.

4. Conclusions

The structural properties of cerium-doped perovskite-type oxides with the formula $Sr_{1-x}Ce_xCo_{0.2}Fe_{0.8}O_{3-\delta}$ for $x = 0.10$, 0.15 and 0.20 have been examined under ambient conditions and at elevated temperatures. All cerium-doped perovskites showed a cubic structure with no observed structural changes/distortions at elevated temperatures. CeO_2 was seen to form a separate phase for dopant concentrations greater than 15%. TEC values calculated from in situ XRD data verified that the Ce-free $SrCoFeO_{3-\delta}$ material to have a much higher thermal expansion coefficient compared to the most commonly used SOFC electrolytes. With increasing cerium dopant concentration, however, thermal compatibility with GDC increased, reaching 16 ppm/°C for SCeCF20.

Although the lowest Ce doping led to the highest oxygen vacancy generation, as seen by the oxygen TPD experiments, this did not directly translate to better button cell performance. The best performance was seen in the intermediate doping levels (15%), which also showed a higher ability for CO_2 dissociation and a higher

intra-facial transport of oxygen, suggesting that CO_2 TPO may serve as a good probe for SOFC performance.

The highest loading level studied (20%) gave the poorest button cell performance as well as the highest area specific resistance as determined by impedance measurements. The presence of a secondary phase with low electrical and/or ionic conductivity, CeO_2, in SCeCF20 may be a factor leading to increased overall impedance and poor button cell performance. This study shows that $SrCoFeO_{3-\delta}$ perovskites with intermediate levels of Ce loading may give optimum levels of oxygen vacancy generation and oxide ion transport while providing TECs comparable to those of the electrolytes and hence may have potential as SOFC cathode materials.

References

[1] H.J.M. Bouwmeester, H. Kruidhof, A.J. Burggraaf, Solid State Ionics 72 (1994) 185.
[2] S. McIntosh, F. Vente Jaap, G. Haije Wim, H.A. Blank Dave, J.M. Bouwmeester Henny, Solid State Ionics 177 (2006) 1737–1742.
[3] R.J.H. Voorhoeve, J.D.W. Johnson, J.P. Remeika, P.K. Gallagher, Science 195 (1977) 827–833.
[4] M.A. Pena, J.L.G. Fierro, Chemical Reviews 101 (2001) 1981.
[5] R.M. Ormerod, Chemical Society Reviews 32 (2003).
[6] C.W. Sun, R. Hui, J. Roller, Journal of Solid State Electrochemistry 14 (2010) 1125–1144.
[7] S.B. Adler, Solid State Ionics 111 (1998) 125.
[8] J. Mizusaki, Y. Mima, S. Yamauchi, K. Fueki, H. Tagawa, Journal of Solid State Chemistry 80 (1989) 102.
[9] J. Mizusaki, M. Yoshihiro, Y.S.K. Fueki, Journal of Solid State Chemistry 58 (1985) 257.
[10] J. Mizusaki, N. Moir, H. Takai, Y. Yonemura, H. Minamiue, H. Tagawa, M. Dokiya, H. Inaba, K. Naraya, T. Sasamoto, T. Hashimoto, Solid State Ionics 129 (2000) 163.
[11] J.N. Kuhn, U.S. Ozkan, Journal of Catalysis 253 (2007) 200–211.
[12] J.N. Kuhn, P.H. Matter, J.-M.M. Millet, R.B. Watson, U.S. Ozkan, Journal of Physical Chemistry 112 (2008) 12468–12472.
[13] J.N. Kuhn, U.S. Ozkan, Catalysis Letters 121 (2008) 179–188.
[14] N. Lakshminarayanan, H. Choi, J.N. Kuhn, U.S. Ozkan, Applied Catalysis B: Environmental 103 (2011) 318–325.
[15] N. Lakshminarayanan, J.N. Kuhn, H. Choi, J.-M.M. Millet, U.S. Ozkan, Journal of Molecular Catalysis A: Chemical 336 (2011) 23–33.
[16] M.T. Colomer, B.C.H. Steele, J.A. Kilner, Solid State Ionics 147 (2002) 41.
[17] L.G. Tejuca, J.L.G. Fierro (Eds.), Properties and Applications of Perovskite-type Oxides, Marcel Dekker, Inc., New York, 1993.
[18] R. Leanza, I. Rossetti, L. Fabbrini, C. Oliva, L. Forni, Applied Catalysis B: Environmental 1 (2000) 55–64.
[19] T. Nitadori, M. Misono, Journal of Catalysis 93 (1984) 459–466.
[20] L. Forni, C. Oliva, T. Barzetti, E. Selli, A.M. Ezerets, A.V. Vishniakov, Applied Catalysis B: Environmental 13 (1997) 35–43.
[21] S.B. Adler, Chemical Reviews 104 (2004) 4791.
[22] S.B. Adler, Journal of the American Ceramic Society 84 (2001) 2117.
[23] T. Selyama, N. Yamazoe, K. Eguchl, Industrial & Engineering Chemistry Product Research and Development 24 (1985) 19–27.
[24] T. Seiyama, N. Yamazoe, K. Eguchi, Industrial and Engineering Chemistry Product Research and Development 24 (1985) 19.
[25] N. Yamazoe, Y. Teraoka, T. Seiyama, Chemistry Letters 12 (1981) 1767.
[26] Y. Teraoka, H.-M. Zhang, N. Yamazoe, Chemistry Letters 9 (1985) 1367–1370.
[27] L.G. Tejuca, J.L.G. Fierro, J.M. Tascon, Advances in Catalysis 36 (1989) 237.
[28] T.-J. Huang, S.-Y. Jhao, Applied Catalysis A: General 302 (2006) 325–332.
[29] T.-J. Huang, X.-D. Shen, C.-L. Chou, Journal of Power Sources 187 (2009) 348–355.